ELSEVIER

Computations of transonic flow with the v^2–f turbulence model

Fue-Sang Lien [a],[*], Georgi Kalitzin [b]

[a] *Department of Mechanical Engineering, University of Waterloo, 200 University Avenue West, Waterloo, Ont., Canada N2L 3G1*
[b] *Department of Mechanical Engineering, Stanford University, Stanford, CA 94305-3030, USA*

Abstract

The v^2–f (or k–ε–$\overline{v'^2}$) model of Durbin, which has shown very good performance in several test cases with separated flows at low speeds, has been applied to transonic flows over the Delery bump and the RAE 2822 airfoil. In both cases, shock-induced separation occurs. The *elliptic relaxation* equation of the model is used in the entire computational domain, i.e., it is computed in both the subsonic and supersonic regimes. The predicted size of the separation zone, surface pressures and mean velocities by two model variants agree reasonably well with the experimental data. Consistent with our earlier investigation, in which the v^2–f model was applied to a subsonic high-lift airfoil at a high incidence angle, the level of turbulent shear–stress within the separation zone is underestimated. A 'code-friendly' variant of the model is proposed to enhance numerical stability. It has proven to be advantageous if an implicit segregated equation-by-equation approach is used. This modification alleviates the 'stiffness problem' associated with the original model caused by the boundary conditions at walls. This is particularly true when the Reynolds number is high and the near-wall grid spacing is extremely small. © 2001 Elsevier Science Inc. All rights reserved.

1. Introduction

Turbulent shock/boundary-layer interaction adjacent to an airfoil's surface has a profound effect on the aerodynamic performance of a transonic aircraft due to the rapid thickening of boundary layers induced by the shock. When the shock is sufficiently strong to provoke boundary-layer separation, a 'λ-shock' structure emanates close to the separation point. This significantly affects the resulting lift and drag coefficients. The simultaneous presence of shear, strong pressure gradient and recirculation-related curvature close to a solid surface leads to a complex, highly anisotropic turbulence structure. Extensive experience with such conditions in incompressible flows suggests that advanced modeling practices, based on second-moment closure, are often necessary for a satisfactory prediction of recirculation. In high-speed aerodynamics, studies of using second-moment closure for shock/boundary-layer interaction problems are rare (e.g., Batten et al., 1997; Ha Minh and Vandromme, 1986; Lien and Leschziner, 1993). The main reason for this is that the Reynolds stress equations do not contain explicitly the second-order fragments representing diffusion, giving rise to poor numerical stability. This problem is further aggravated when all Reynolds-stress components are stored at the same location. Checkerboard oscillations result from *velocity–stress* decoupling. In Lien and Leschziner (1994),

this problem has been overcome through the introduction of a fourth-order smoothing term, while stresses at each face are interpolated. Another difficulty associated with the numerical implementation of second-moment closure is its boundary conditions on a curved surface. Since most of the recent low-*Re* second-moment closure models (such as Craft and Launder, 1996) are highly sophisticated and have been validated only for a range of simple flows, the common practice is to interface the high-*Re* second-moment closure (such as Gibson and Launder, 1978) with any standard low-*Re* eddy-viscosity model at the location where $y^+ \approx 60$.

However, most of the low-*Re* k–ε models reviewed by Patel et al. (1985) contain an ad hoc viscous damping function f_μ in the eddy-viscosity expression, i.e.,

$$v_t = f_\mu C_\mu k T, \tag{1}$$

which corrects the improper asymptotic behavior of the eddy-viscosity formulation when approaching a solid wall. The damping function is often non-linear and causes numerical stiffness. Since the primary objective of introducing the damping effect to closure models is to represent the *kinematic blocking* by the wall, Durbin (1991) suggested that $\overline{v'^2}$ – regarded as the turbulence stress normal to streamlines – rather than k should be used in Eq. (1). As a result, no viscous-damping function is required in his v^2–f model. The quantity $\overline{v'^2}$ is obtained from a transport equation simplified from second-moment closure. The associated pressure–strain term in the $\overline{v'^2}$-equation, a term responsible for redistribution of turbulence energy in the proximity of walls in order to return the correct level of turbulence anisotropy, is obtained from an auxiliary *elliptic relaxation* equation. The v^2–f model, includ-

[*] Corresponding author. Tel.: +1-519-888-4567; fax: +1-519-888-6197.
E-mail addresses: fslien@sunwise.uwaterloo.ca (F.-S. Lien), kalitzin@stanford.edu (G. Kalitzin).

ing its variants, has been validated over a wide range of incompressible flows (e.g., Durbin, 1995; Perneix et al., 1998). Only very recently, the model was applied to a transonic airfoil (Lien et al., 1998) using a high-speed density-based code in order to investigate whether the 'elliptic relaxation' model can still be used when a flow becomes supersonic.

The objective of this paper is to report a continuous effort in which the same model is applied to transonic flows over the Delery bump (Delery, 1983) and the RAE 2822 airfoil (Cook et al., 1979). Detailed experimental data are available for both cases so that the performance of the v^2–f model can be assessed properly.

2. v^2–f turbulence model

2.1. Original model (Durbin, 1995)

The Boussinesq approximation is used for the stress–strain relation

$$\frac{\overline{u'_i u'_j}}{k} - \frac{2}{3}\delta_{ij} = -\frac{v_t}{k}\left(\frac{\partial u_i}{\partial x_j} + \frac{\partial u_j}{\partial x_i}\right). \tag{2}$$

The eddy-viscosity v_t is given by

$$v_t = C_\mu \overline{v'^2} T. \tag{3}$$

The turbulent time scale T

$$T = \min\left[\max\left[\frac{k}{\epsilon}, 6\sqrt{\frac{v}{\epsilon}}\right], \frac{0.6k}{\sqrt{6}C_\mu \overline{v'^2} S}\right] \tag{4}$$

and the turbulent length scale L

$$L = C_L \max\left[\min\left[\frac{k^{3/2}}{\epsilon}, \frac{k^{3/2}}{\sqrt{6}C_\mu \overline{v'^2} S}\right], C_\eta \frac{v^{3/4}}{\epsilon^{1/4}}\right] \tag{5}$$

are determined from the standard k–ε equations

$$\frac{\partial k}{\partial t} + u_j \frac{\partial k}{\partial x_j} = P_k - \varepsilon + \frac{\partial}{\partial x_j}\left[\left(v + \frac{v_t}{\sigma_k}\right)\frac{\partial k}{\partial x_j}\right], \tag{6}$$

$$\frac{\partial \varepsilon}{\partial t} + u_j \frac{\partial \varepsilon}{\partial x_j} = \frac{C_{\varepsilon 1}P_k - C_{\varepsilon 2}\varepsilon}{T} + \frac{\partial}{\partial x_j}\left[\left(v + \frac{v_t}{\sigma_\varepsilon}\right)\frac{\partial \varepsilon}{\partial x_j}\right]. \tag{7}$$

The strain-rate magnitude S is defined as $S = \sqrt{S_{ij}S_{ij}}$ with $S_{ij} = 0.5(\partial u_i/\partial x_j + \partial u_j/\partial x_i)$. v is the kinematic viscosity and $P_k = -\overline{u'_i u'_j}\partial u_i/\partial x_j$ is the production of turbulent kinetic energy. Denoting with y the coordinate normal to the wall, on no-slip boundaries, $y \to 0$, yields

$$k = 0, \quad \varepsilon \to 2v\frac{k}{y^2}. \tag{8}$$

The $\overline{v'^2}$ transport equation is

$$\frac{\partial \overline{v'^2}}{\partial t} + u_j \frac{\partial \overline{v'^2}}{\partial x_j} = \underline{kf - \overline{v'^2}\frac{\varepsilon}{k}} + \frac{\partial}{\partial x_j}\left[\left(v + \frac{v_t}{\sigma_k}\right)\frac{\partial \overline{v'^2}}{\partial x_j}\right], \tag{9}$$

where

$$kf = \underbrace{\phi_{22}}_{\text{pressure strain}} - \underbrace{\varepsilon_{22}}_{\text{dissipation}} + \frac{\overline{v'^2}}{k}\varepsilon \tag{10}$$

represents the redistribution of turbulence energy from the streamwise component. Non-locality is represented by solving an *elliptic relaxation* equation for f

$$L^2 \frac{\partial^2 f}{\partial x_j^2} - f = \frac{1}{T}(C_1 - 1)\left[\frac{\overline{v'^2}}{k} - \frac{2}{3}\right] - C_2 \frac{P_k}{k}. \tag{11}$$

The asymptotic behavior of the pressure–strain ϕ_{22} and the dissipation term ε_{22} near a wall are (Mansour et al., 1988)

$$\phi_{22} = -2\frac{\overline{v'^2}}{k}\varepsilon, \quad \varepsilon_{22} = 4\frac{\overline{v'^2}}{k}\varepsilon. \tag{12}$$

This yields the boundary condition for f in the original v^2–f model

$$kf(0) \to -5\frac{\overline{v'^2}}{k}\varepsilon \quad \text{or} \quad f(0) \to -\frac{20v^2\overline{v'^2}}{\varepsilon(0)y^4}. \tag{13}$$

The coefficients of the original model, denoted by 'Model 1' in Section 4, are

$$C_\mu = 0.19, \quad \sigma_k = 1, \quad \sigma_\epsilon = 1.3,$$

$$C_{\epsilon 1} = 1.3 + 0.25/\left[1 + (C_L d/2L)^2\right]^4, \quad C_{\epsilon 2} = 1.9,$$

$$C_1 = 1.4, \quad C_2 = 0.3, \quad C_L = 0.3, \quad C_\eta = 70,$$

where d is the distance to the wall.

2.2. Code-friendly variant (Lien and Durbin, 1996; Lien et al., 1998)

The boundary condition for f, i.e., Eq. (13), involves y^4 and $\varepsilon(0)$ in the denominator. The latter is ill defined in the laminar and transitional regions, giving rise to numerical oscillations as illustrated in Fig. 1 for flow over a flat plate. These oscillations are mainly encountered when a segregated numerical procedure is adopted which does not allow an implicit coupling between $\overline{v'^2}$ and f at the wall. This inspired a reformulation of the underlined term of Eq. (9)

$$\underbrace{\phi_{22} - \varepsilon_{22} + 6\frac{\overline{v'^2}}{k}\varepsilon}_{=kf} - 6\frac{\overline{v'^2}}{k}\varepsilon, \tag{14}$$

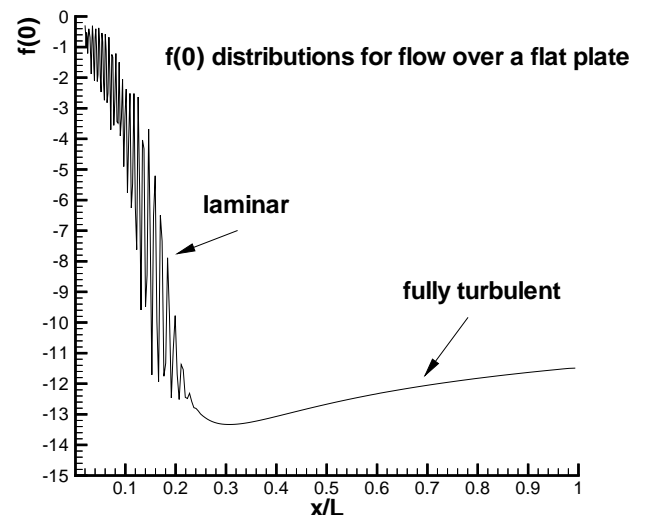which changes the definition of f, and therefore, the elliptic relaxation equation

Fig. 1. Distribution of $f(0)$ for a flow over a flat plate (Lien and Leschziner, 1993).

$$L^2 \frac{\partial^2 f}{\partial x_j^2} - f = \frac{1}{T}\left[(C_1 - 6)\frac{\overline{v'^2}}{k} - \frac{2}{3}(C_1 - 1)\right] - C_2 \frac{P_k}{k}. \quad (15)$$

According to Eqs. (12) and (14), the boundary condition for f at the wall results in $f(0) = 0$, which greatly enhances the numerical stability. Note that such a modification retains the same asymptotic near-wall behavior of $\overline{v'^2}$ as in the original model: $\overline{v'^2} \sim y^4$ as $y \to 0$. As $y \to \infty$, the kinematic blocking effect arising from 'elliptic relaxation' disappears. Both $kf - (\overline{v'^2}/k)\varepsilon$ in Eq. (9) and $kf - 6(\overline{v'^2}/k)\varepsilon$ in Eq. (14) are identical and equal to

$$-C_1 \frac{\varepsilon}{k}\left(\overline{v'^2} - \frac{2}{3}k\right) + C_2 P_k - \frac{2}{3}\varepsilon. \quad (16)$$

Eq. (15) can also be derived from the original model by substituting f in Eq. (11) with a new variable $f^* - 5\epsilon\overline{v'^2}/k^2$ and neglecting the term $-5L^2(\partial^2/\partial x_j^2)(\overline{v'^2}/k^2)$, which appears in the transformed f^*-equation. The ratio k/ϵ appearing in the same f^*-equation is substituted with the time scale T.

The constants of the resulting code-friendly model, denoted by 'Model 2' in Section 4, are

$$C_\mu = 0.22, \quad \sigma_k = 1, \quad \sigma_\varepsilon = 1.3,$$

$$C_{\varepsilon1} = 1.4\left(1 + 0.050\sqrt{k/\overline{v'^2}}\right), \quad C_{\varepsilon2} = 1.9,$$

$$C_1 = 1.4, \quad C_2 = 0.3, \quad C_L = 0.23, \quad C_\eta = 70. \quad (17)$$

Note that all model constants in Eq. (17) are completely *wall distance independent*, i.e., not dependent on $y^+(= yu_\tau/v)$ or $y^*(= y\sqrt{k}/v)$ as in most of the low-Re k–ε models. Therefore, the model is not only numerically friendly but ideal for block-structured and unstructured-grid methods including their parallelization.

The model described has been validated against a fully developed channel flow at $Re_\tau = 395$ and, as seen in Fig. 2, the predicted turbulent profiles of k, ε, $\overline{v'^2}$ agree reasonably well with the DNS data of Kim et al. (1987).
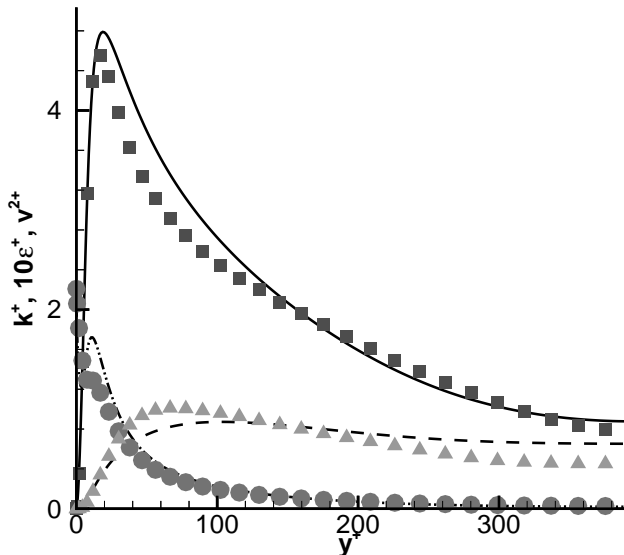

Fig. 2. Profiles of k, ε, $\overline{v'^2}$ for channel flow. — k^+ (comp); $-\cdot-$ $10\varepsilon^+$ (comp); - - - $\overline{v'^2}^+$ (comp); ■ k^+ (DNS); ● $10\varepsilon^+$ (DNS); ▲ $\overline{v'^2}^+$ (DNS).

3. Numerical methods

Two different numerical algorithms are adopted here. The first is a pressure-based scheme which is used for the Delery bump computations. The second is a density-based method which is used for the RAE 2822 computations. Details are summarized as follows.

STREAM (Lien and Leschziner, 1994) is a general geometry, block-structured, finite-volume code developed at UMIST. [1] Advection is approximated by TVD or QUICK scheme. To avoid checkerboard oscillations within the collocated storage arrangement, the 'Rhie and Chow' interpolation method (Rhie and Chow, 1983) is used. The solution is effected by an iterative pressure-correction SIMPLE algorithm for incompressible flows. To extend this algorithm to transonic regimes, the 'retarded-density' concept, originally developed for solving the full potential equation, has been introduced into the present pressure-correction scheme (Hafez et al., 1979; Lien and Leschziner, 1993; Lien, 2000).

CFL3D (Krist et al., 1998), a density-based code developed at NASA, solves the time-dependent thin-layer RANS equations using multiblock-structured grids. A semi-discrete finite-volume approach is used for the spatial discretization. The convective and diffusion terms are discretized with a third-order upwind and a central difference stencil, respectively. The code uses flux-difference splitting based on the Roe-scheme with a smooth flux limiter. Time advancement is implicit. A three-factored approximate factorization scheme is used to invert the matrices, resulting from the implicit operator. The steady-state computations have been performed by marching in time from an initial guess. To accelerate convergence, local time stepping is used for all variables both mean flow and turbulence, while multigrid is used only for the mean flow.

4. Results and discussion

4.1. Delery transonic bump

To investigate the performance of the v^2–f model when applied to transonic conditions, the transonic bump flow of Delery (1983) – Delery's Case C – was chosen due to the wealth of related LDA experimental data. Calculations reported below have been performed with 210×90 and 420×180 nodes, and only the former is shown in Fig. 3. The near-wall grid is arranged so as to give a y^+ value of order 1 along the grid line closest to the wall. The density at the inlet is extrapolated from the interior solution domain, and the pressure at the same location is extracted from the appropriate isentropic relation using the stagnation condition: $T_0 = 300$ K and $P_0 = 96000 Pa$ from the experiment. The velocity is then obtained from the condition of invariant total enthalpy. At the outlet, the exit pressure has been adjusted so that the shock wave which develops on the lower wall coincides reasonably well with that in the experiment. This is, essentially, a trial-and-error exercise, depending on the turbulence model used (Batten et al., 1997). Thus, the exit pressures for the computations with Models 1 and 2 differ slightly.

The resulting wall pressure distributions, obtained with both 210×90 and 420×180 nodes, are shown in Fig. 4. As seen, even the coarser grid supports the grid independent solutions. The 'pressure plateau' observed in the figure indicates the presence of a separation bubble as a result of strong shock/boundary-layer interaction. The pressure recovery in Model 1
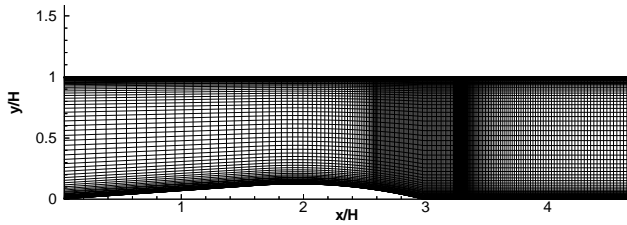

Fig. 3. Delery bump: computational mesh containing 210×90 nodes.
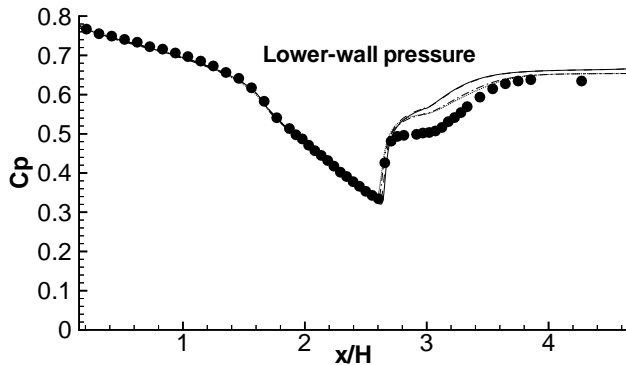
Fig. 4. Delery bump: pressure distributions. — 420×180 - - - 210×90, Model 1; – · – 420×180, · · · 210×90, Model 2; ∘ expt.

Fig. 5. Delery bump: Mach-number contours obtained with 420×180 nodes.

Fig. 6. Delery bump: streamline contours obtained with 420×180 nodes.

is faster than that in Model 2, which influences the thickness of the bubble as discussed later. In both cases, the wall pressures after the shock, particularly within the separation region, are higher than in the experiment. This implies that the 'three-dimensional blockage' effect arising from boundary layers on the side walls of the wind tunnel might be important here.

The corresponding Mach-number contours obtained with both models are given in Fig. 5, in which an oblique shock emanating in the vicinity of separation point is seen to merge with the normal shock approximately in the middle of channel at $x/H \approx 3$. It can be seen from Figs. 4 and 5 that the separation points predicted by both models are fairly close to the foot of the λ-shock.

Comparisons between the predicted separation and reattachment points, obtained with both models, and the experimental data are given in Figs. 6 and 7 and Table 1. As seen, the predicted separation points returned by both models: $x_S/H = 2.69$ for Model 1 and $x_S/H = 2.72$ for Model 2 agree reasonably well with the experimental values: $x_S/H = 2.73$. It is our experience from many other incompressible flows that Model 2 tends to predict a slightly higher level of the wall shear–stress than Model 1, and this trend has also been observed for the RAE 2822 transonic airfoil test case discussed in Section 4.2. The separation point predicted by Model 2 is in good agreement with the experimental value in the present case, and the separation point computed with Model 1 is slightly upstream. Both models underpredict the reattachment length by a factor of about 10% according to the experiment.

A selection of velocity and turbulent shear–stress profiles are given in Figs. 8 and 9, which serve to reinforce previous observations. The shear–stress level obtained with Model 2 is lower than that returned by Model 1 within the separation zone, i.e., at $x/H = 2.81$ and 3.02. As a result of a lower level of shear–stress and, hence, a lower rate of fluid entrainment, the separation bubble predicted by Model 2 should be thicker; this is what we observed in Fig. 6. Further downstream of the
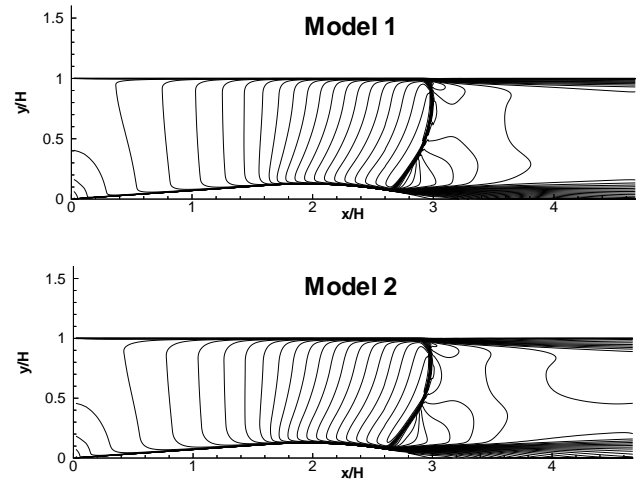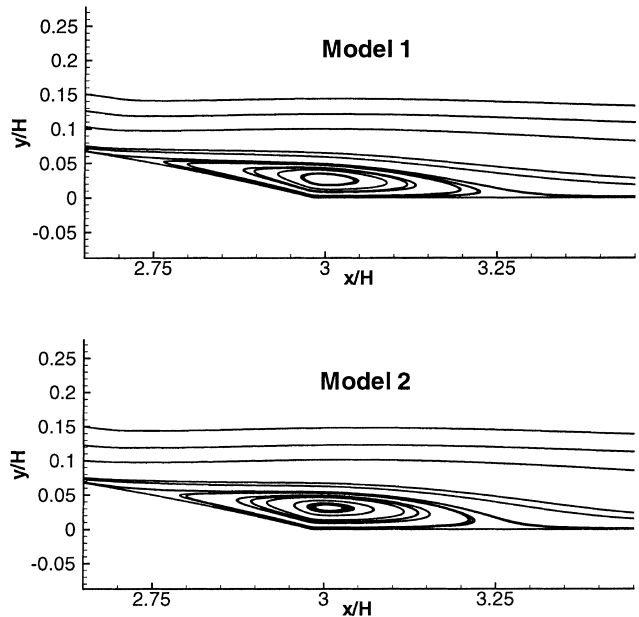
reattachment point at $x/H = 3.44$, Model 1 predicts a faster recovery as shown in Fig. 8. This is consistent with a faster pressure recovery observed earlier in Fig. 4 with the same model.

Our experience in applying v^2–f model variants to incompressible separated flows over curved surfaces, both in 2D and 3D (Lien and Durbin, 1996), did demonstrate that the model performed better than most conventional low-Re eddy-viscosity models, which involve a viscous-damping function f_μ. The predicted turbulent shear–stress profiles within the separation zone in the present study, shown in Fig. 9, and in Lien and Durbin (1996) are consistently underestimated in comparison with the experimental data, regardless of whether the flow is incompressible or transonic involving shock waves. In Section 5, possible explanations and remedies will be suggested.
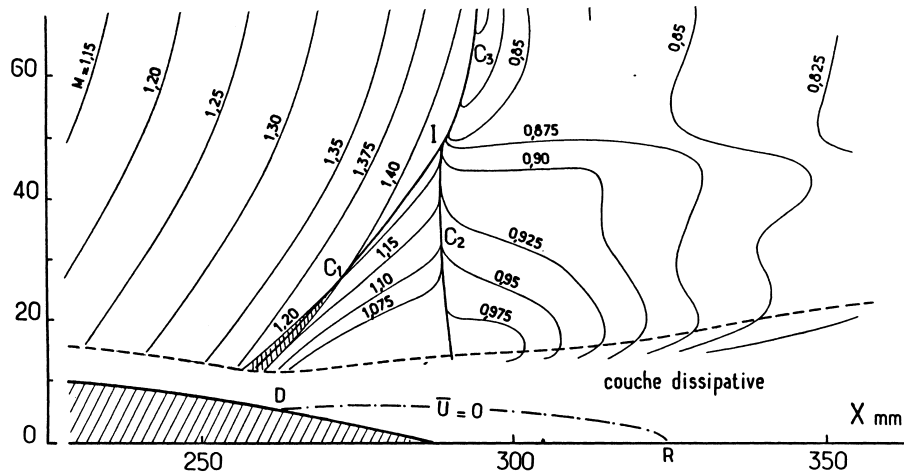
Fig. 7. Experimental data of Mach-number contours and separation lines (Delery, 1983). $H = 96$ mm.

Table 1
Comparison between predicted separation and reattachment points and the experimental data[a]

	Separation point	Reattachment point
Model 1	$x_S/H = 2.69$	$x_R/H = 3.30$
Model 2	$x_S/H = 2.72$	$x_R/H = 3.28$
Experiment	$x_S/H = 2.73$	$x_R/H = 3.38$

[a] $H = 96$ mm is the channel height.

4.2. RAE 2822 transonic airfoil

Transonic flow around the supercritical RAE 2822-airfoil for cases 9 and 10 flow conditions (Cook et al., 1979) is the second test case involving shock/boundary layer interaction. The flow conditions for these cases differ only slightly in Mach number and Reynolds number. While in case 9, the shock is too weak to induce separation, the flow separates at the shock location for case 10. The amount of separation and the position of the shock are highly sensitive to the turbulence level generated.

The experimental data were obtained in the wind tunnel for the flow conditions: case 9: $M_\infty = 0.73$, $Re = 6.50 \times 10^6$,
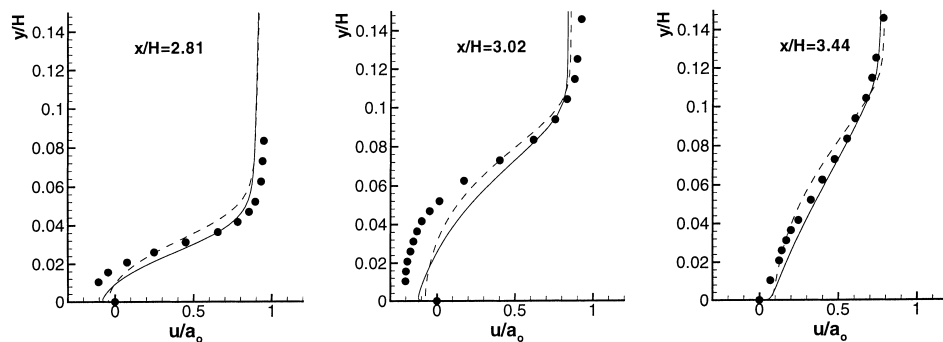

Fig. 8. Delery bump: streamwise velocity profiles obtained with 420×180 nodes. — Model 1; - - - Model 2; ○ expt.
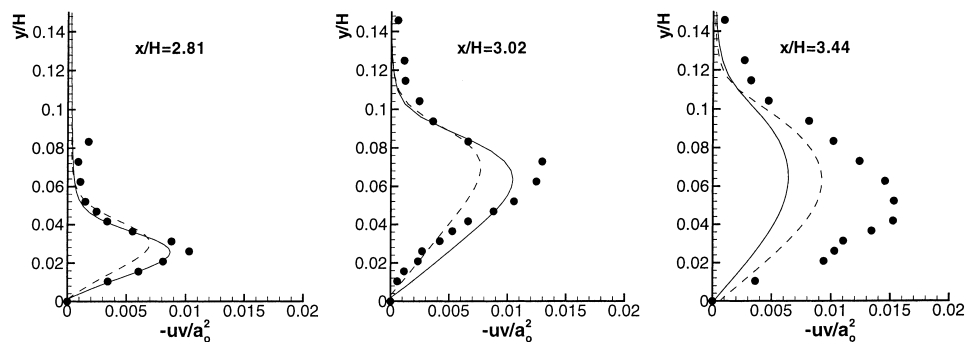

Fig. 9. Delery bump: turbulent shear–stress profiles obtained with 420×180 nodes. — Model 1; - - - Model 2; ○ expt.

Fig. 10. RAE 2822 airfoil: pressure and skin friction distribution for case 9. — 256 × 64, — 512 × 128, Model 1; - - - 256 × 64, - - - 512 × 128, Model 2; ○ expt.

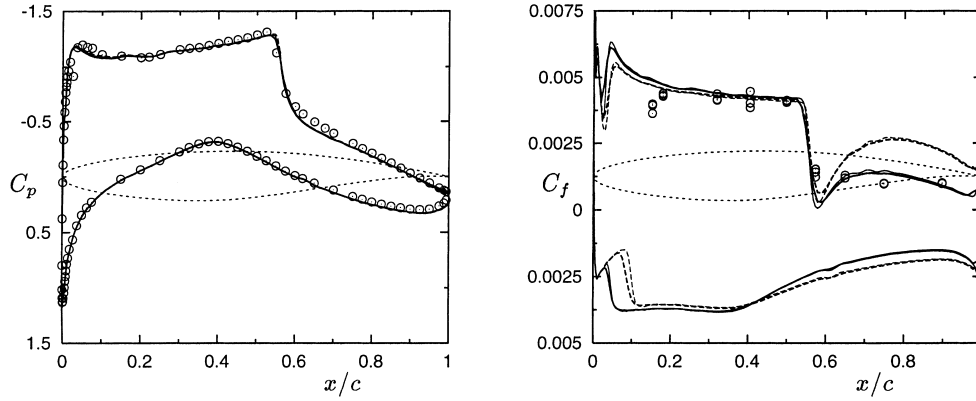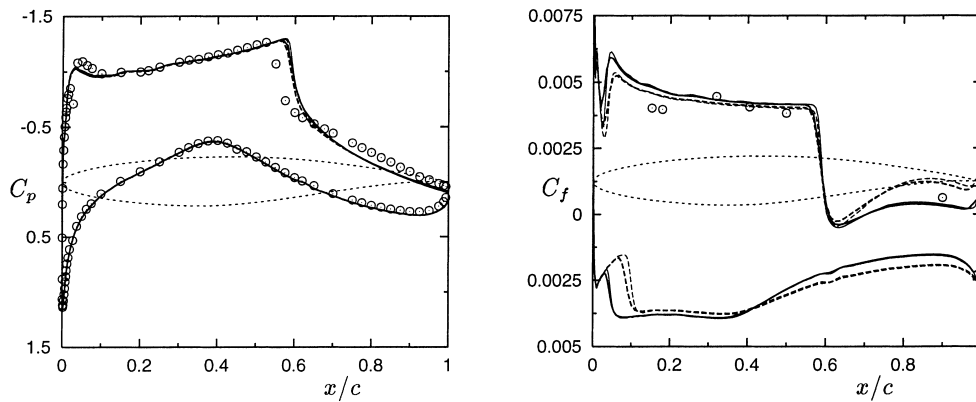Fig. 11. RAE 2822 airfoil: pressure and skin friction distribution for case 10. — 256 × 64, — 512 × 128, Model 1; - - - 256 × 64, - - - 512 × 128, Model 2; ○ expt.

α=3.19° and case 10: M_∞=0.75,Re=6.20×10⁶,α=3.19°. In the experiments, transition has been tripped near the leading edge of the airfoil at x/c=0.03 on both upper and lower surfaces of the airfoil.

To compare the experimental data with a flow around an airfoil in free-flight conditions, corrections to the tunnel data are required. Different wind tunnel corrections have been used in various studies published in the literature (Haase et al., 1993; Krist et al., 1998). The flow conditions used in the EUROVAL project (Haase et al., 1993) are adopted here. They are $M_\infty = 0.734$, $Re = 6.50 \times 10^6$, α = 2.54 and $M_\infty = 0.754$, $Re = 6.20 \times 10^6$, α = 2.57 for cases 9 and 10, respectively. Note that for case 10 in particular, researchers tend to compute the flow with a slightly higher angle of attack. Clearly, this influences the location of the shock. The shock location and the pressure distribution, particularly on the suction side, are influenced by the outer extent of the computational domain. The finite far field boundary causes a lower circulation around the airfoil, leading to an underprediction of lift. A vortex correction to the far-field boundary condition adjusts the circulation around the airfoil and, therefore, has been employed for the present computations.

The present computations were carried out with two meshes used in Haase et al. (1993). The finer mesh consists of 512 × 128 nodes and has 384 nodes on the airfoil surface. The average y^+ value of the first node above the wall is about 0.5. The coarser mesh has been obtained by omitting every second grid line. Thus, it consists of 256 × 64 nodes and has 192 nodes
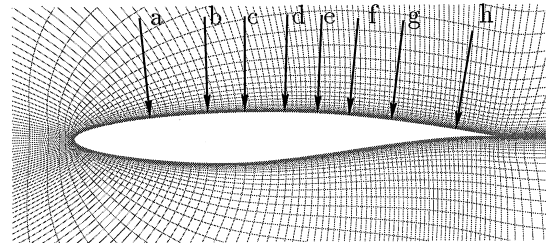

Fig. 12. RAE 2822 airfoil: computational mesh containing 256 × 64 nodes. x/c = 0.179 (a), 0.319 (b), 0.404 (c), 0.498 (d), 0.574 (e), 0.650 (f), 0.750 (g), 0.900 (h).

on the airfoil surface. For this mesh, the average y^+ value of the first cell above the wall is about 1. The coarse mesh near the airfoil is shown in Fig. 12. The far field is about 15 cord lengths from the airfoil.

In the computation, transition is modeled in a crude way by switching off turbulence production terms upstream of transition. The stagnation point anomaly does not appear for airfoil flow computations with fixed transition. The upper bounds on the time and length scales in Eqs. (4) and (5) which were designed to ensure realizability of the v^2–f model in stagnation regions (Durbin, 1996) are therefore not needed. However, tests with the upper bounds were performed and identical mean flow results were obtained.

Pressure and skin friction distributions are shown in Figs. 10 and 11 for cases 9 and 10, respectively. The airfoil contour is shown with a thin dashed line in the middle of the plots. As commonly plotted in aerospace industry, the C_f axis for skin friction on the lower surface of the airfoil and the C_p axis for pressure on both surfaces are reversed. Thus, the upper part of pressure and skin friction distributions correspond to the results on the upper surface of the airfoil and the lower part of the distributions correspond to the results on the lower surface of the airfoil. Thicker lines are used for the results on a coarser mesh containing 256×64 nodes. A mesh of this size is usually used for 2D computations.

Velocity profiles are shown in Figs. 13 and 14 for both cases. The profiles are taken normal to the airfoil surface. The

location of the stations considered is shown in Fig. 12. Note that in Cook et al. (1979), the experimental data for the skin friction and velocity are normalized by the velocity at the edge of the boundary layer. Here, it has been rescaled with the free-stream velocity.

The results obtained on the two different meshes are reasonably grid independent for both test cases. On the finer mesh, the shock is slightly sharper and the skin friction rises more rapidly at transition. The skin friction tends to be slightly lower at the shock foot which for case 10 corresponds to an increased flow recirculation.

The pressure distributions and velocity profiles agree quite well with the experimental data for case 9. For case 10, however, the shock, which is located on the upper surface of the
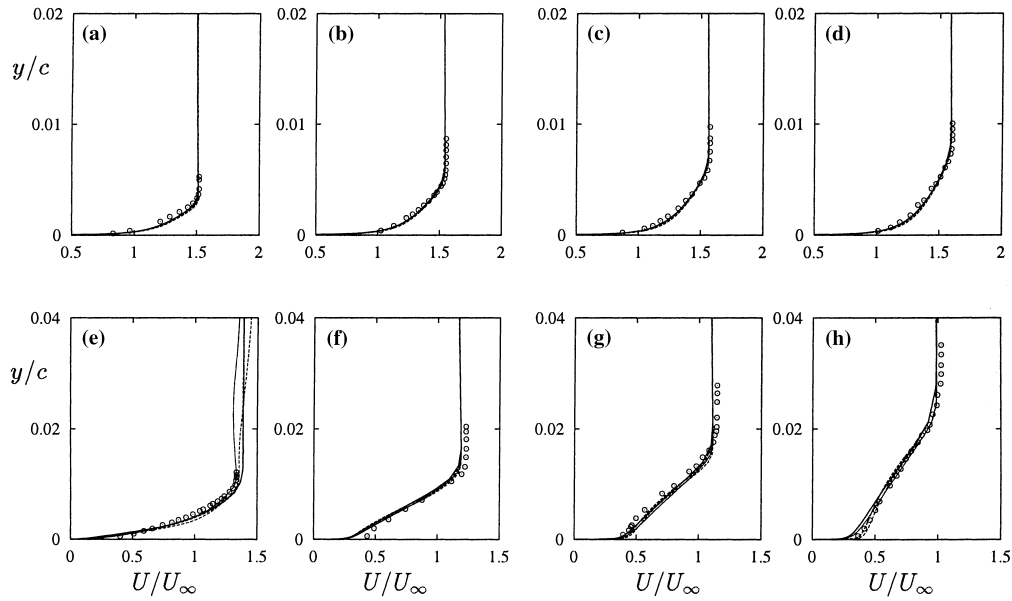

Fig. 13. RAE 2822 airfoil: velocity profiles for case 9. — 256×64, — 512×128, Model 1; - - - 256×64, - - - 512×128, Model 2; ○ expt (see location of stations in Fig. 12).
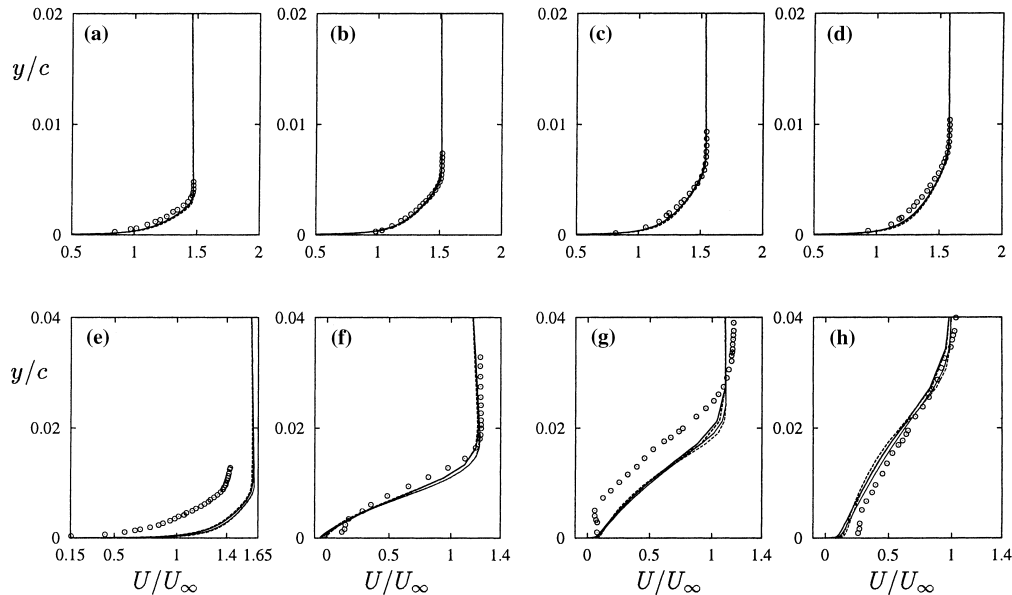
Fig. 14. RAE 2822 airfoil: velocity profiles for case 10. — 256×64, — 512×128, Model 1; - - - 256×64, - - - 512×128, Model 2; ○ expt (see location of stations in Fig. 12).

airfoil at around $x/c = 0.55$ according to the experiment, is too far downstream indicating that the growth rate of the boundary layer is too slow. While the velocity profiles at the stations upstream of the shock agree quite well with the experiment, the discrepancy between numerical and experimental data increases downstream. The slow growth of the boundary layer is particularly visible in the velocity profile at station e, which is located close to the shock.

While the difference in pressure distributions and shock locations between both models is quite small, it becomes more apparent in the skin friction data. For case 9, Model 2 predicts a significantly larger skin friction on the upper surface of the airfoil downstream of the shock. This corresponds to a larger velocity gradient at the wall, e.g., at stations g and h shown in Fig. 13. Model 2 also predicts a larger skin friction on the lower surface of the airfoil as shown in Figs. 10 and 11. Consistent with earlier computations, Model 2 delays the growth of the turbulent boundary layer at transition.

The lift and drag coefficients for cases 9 and 10 are given in table below. In particular, for case 10, Model 2 predicts values which are slightly closer to the experimental data.

	Case 9	
	C_L	C_D
Model 1 (512×128)	0.7966	0.01641
Model 1 (256×64)	0.8009	0.01734
Model 2 (512×128)	0.8053	0.01672
Model 2 (256×64)	0.8028	0.01750
Experiment	0.803	0.0168
	Case 10	
	C_L	C_D
Model 1 (512×128)	0.7610	0.02555
Model 1 (256×64)	0.7600	0.02624
Model 2 (512×128)	0.7535	0.02497
Model 2 (256×64)	0.7493	0.02554
Experiment	0.743	0.0242

There are two major differences between Models 1 and 2. One is obviously the modification of the boundary condition at walls which, in the present computations, is believed to affect mainly the skin friction in recovery regions on the upper surface of the airfoil downstream of the shock. The second difference is the definition of the coefficient $C_{\epsilon 1}$, which determines the production of dissipation. While Model 1 uses the distance to walls to vary this coefficient between 1.55 near the wall and 1.3 in the outer part of the boundary layer, Model 2 uses the ratio of $\overline{v^2}/k$ to vary this coefficient, which is estimated to be around 1.45 in the entire boundary layer. The higher value of $C_{\epsilon 1}$ over most parts of the boundary layer leads to a stronger tendency of flow separation for Model 2 or, as shown in Kalitzin (1999b), for Model 1 with a similar $C_{\epsilon 1}$ definition.

Comparisons between the v^2–f model, the Spalart–Allmaras model and Menter's SST model for cases 9 and 10 are published in Kalitzin (1999a) and Kalitzin (1999b). Note that some of the coefficients for the v^2–f model employed earlier may differ from those used in the present study.

5. Conclusions

The v^2–f model has been used to solve Delery's transonic bump flow. Although 2D calculations were performed here, our early work (Lien and Leschziner, 1993) reported that the predictions were contaminated, to some degree, by 3D features arising from boundary layers developing on side walls. As the formation of a λ-shock is due to compression waves emanating from the separation point, the performance of the turbulence model depends crucially on its ability to respond to adverse pressure gradients caused by the bump geometry and the shock penetrating into the boundary layer. The separation points predicted by both models agree very well with the experimental data. However, the reattachment length is too short. The predicted maximum 'negative' velocity is slightly too low, suggesting an underestimation of the shear–strain $\partial u/\partial y$ and, hence, the shear–stress $-\overline{u'v'}$. A similar deficiency in terms of turbulent shear–stress within the recirculation region has also been noticed for an incompressible flow over a high-lift airfoil at a high angle of attack (Lien and Durbin, 1996). This might be attributed to the production term in the $\overline{v'^2}$-equation being omitted – a key assumption in the v^2–f model which decouples $\overline{v'^2}$ from $\overline{u'^2}$ and $\overline{w'^2}$ when a flow is fully developed. However, such an approximation is not entirely correct along a curved shear layer emanating from the separation point. In order to capture the correct behavior of near-wall turbulence anisotropy, both the v^2–f model with a non-linear stress–strain constitutive relation and the low-Re Reynolds-stress model of Durbin (1993) will be considered and results will be reported in future accounts.

The results for the RAE 2822 airfoil show that despite the ellipticity of the f-equation and the presence of strong shock waves in the flow, the v^2–f model is able to predict transonic flows accurately. The pressure and skin friction distributions as well as velocity profiles predicted by both models in most parts of the flow are of similar quality. Larger differences can be observed once the flow separates. The error introduced in transonic flows by the integration of the f-equation over the whole computational domain rather than over its true domain of dependence does not seem to influence the mean flow, at least for the test cases considered here. The eddy-viscosity depends on $\overline{v'^2}$ and, hence, indirectly on f, with f representing the only production term in the v^2 equation. In addition, this term is scaled by the turbulent kinetic energy k. Towards the edge of boundary layers, k decays rapidly towards its freestream value, which is very small.

References

Batten, P.E., Loyau, H., Leschziner, M.A., 1997. In: Proceedings of the Workshop on Shock/Boundary-Layer Interaction, UMIST, UK.

Craft, T.J., Launder, B.E., 1996. A Reynolds stress closure designed for complex geometries. Int. J. Heat Fluid Flow 17, 245.

Cook, P.H., McDonald, M.A., Firmin, M.C.P., 1979. Aerofoil 2822-pressure distributions, boundary layer and wake measurements, AGARD AR 138.

Delery, J.M., 1983. Experimental investigation of turbulence properties in transonic shock-wave/boundary-layer interactions. AIAA J. 21, 180.

Durbin, P.A., 1991. Near-wall turbulence closure modelling without damping function. Theor. Comput. Fluid Dynamics 3, 1.

Durbin, P., 1993. A Reynolds stress model for near-wall turbulence. J. Fluid. Mech. 249, 465.

Durbin, P.A., 1995. Separated flow computations with the k–ε–v^2 model. AIAA J. 33, 659.

Durbin, P., 1996. On the k–ϵ stagnation point anomaly. Int. J. Heat Fluid Flow 17, 89.

Gibson, M.M., Launder, B.E., 1978. Ground effects on pressure fluctuations in the atmospheric boundary layer. J. Fluid Mech. 86, 491.

Haase, W., Bradsma, F., Elsholz, E., Leschziner, M., Schwamborn, D., 1993. EUROVAL – an European Initiative on Validation of CFD Codes Notes on Numerical Fluid Mechanics, Vieweg, p. 42.

Hafez, M., South, J., Murman, E., 1979. Artificial compressibility methods for numerical solutions of transonic full potential equation. AIAA J. 17, 838.

Ha Minh, H., Vandromme, D.D., 1986. Modelling of compressible turbulent flows: present possibilities and perspectives. In: Proceedings of the Shear Layer/Shock Wave Interaction, IUTAM Symposium, Palaiseau, Springer, Berlin, p. 13.

Kalitzin, G., 1999a. Application of v^2–f turbulence model to transonic flows, AIAA-99-3780.

Kalitzin, G., 1999b. Application of the v^2–f model to aerospace configurations, CTR - Annual Research Briefs.

Kim, J., Moin, P., Moser, R.D., 1987. Turbulence statistics in fully-developed channel flow at low Reynolds number. J. Fluid Mech. 177, 133.

Krist, S., Biedron, R., Rumsey, C., 1998. CFL3D User's Manual, Version 5.0, NASA/TM-208444.

Lien, F.S., 2000. A pressure-based unstructured grid method for all-speed flows. Int. J. Numer. Meth. Fluids 33, 355.

Lien, F.S., Durbin, P.A., 1996. Non-linear k–ε–$\overline{v^2}$ modelling with application to high lift. In: Proceedings of the Summer Program 1996, Stanford University, p. 5.

Lien, F.S., Kalitzin, G., Durbin, P.A., 1998. RANS modelling for compressible and transitional flows. In: Proceedings of the Summer Program 1998, Stanford University, p. 267.

Lien, F.S., Leschziner, M., 1993. A pressure–velocity solution strategy for compressible flow and its application to shock/boundary-layer interaction using second-moment turbulence closure. ASME J. Fluid Eng. 115, 717.

Lien, F.S., Leschziner, M.A., 1994. A general non-orthogonal collocated finite volume algorithm for turbulent flow at all speeds incorporating second-moment closure, part 1: computational implementation, part 2: application. Comput. Meth. Appl. Mech. Eng. 114, 123.

Mansour, N.N., Kim, J., Moin, P., 1988. Reynolds-stress and dissipation-rate budgets in a turbulent channel flow. J. Fluid Mech. 194, 15.

Patel, V.C., Rodi, W., Scheuerer, G., 1985. Turbulence models for near-wall and low Reynolds number flows: a review. AIAA J. 23, 1308.

Perneix, S., Durbin, P.A., Behnia, M., 1998. Computation of 3-D turbulent boundary layers using the v^2–f model. Flow Turbul. Combust. 10, 19.

Rhie, C.M., Chow, W.L., 1983. Numerical study of the turbulent flow past an airfoil with trailing edge separation. AIAA J. 21, 1525.